Photoelectric conversion on Earth's surface via widespread Fe- and Mn-mineral coatings

Anhuai Lu[a,b,c,1,2], Yan Li[a,b,1,3], Hongrui Ding[a,b,1], Xiaoming Xu[a,b], Yanzhang Li[a,b], Guiping Ren[a,b], Jing Liang[d], Yuwei Liu[a,b], Hao Hong[d], Ning Chen[e], Shengqi Chu[f], Feifei Liu[a,b], Yan Li[a,b,4], Haoran Wang[a,b], Cong Ding[a,b], Changqiu Wang[a,b], Yong Lai[a,b], Juan Liu[a,g], Jeffrey Dick[c], Kaihui Liu[d,2], and Michael F. Hochella Jr.[h,i,2]

[a]Beijing Key Laboratory of Mineral Environmental Function, School of Earth and Space Sciences, Peking University, 100871 Beijing, People's Republic of China; [b]The Key Laboratory of Orogenic Belts and Crustal Evolution, School of Earth and Space Sciences, Peking University, 100871 Beijing, People's Republic of China; [c]The Key Laboratory of Metallogenic Prediction of Nonferrous Metals and Geological Environment Monitoring, School of Geosciences and Info-Physics, Central South University, 410083 Changsha, People's Republic of China; [d]State Key Laboratory for Mesoscopic Physics, Collaborative Innovation Center of Quantum Matter, School of Physics, Peking University, 100871 Beijing, People's Republic of China; [e]Hard X-ray MicroAnalysis (HXMA) Beamline, Canadian Light Source, Saskatoon, SK S7N 2V3, Canada; [f]Beijing Synchrotron Radiation Facility, Institute of High Energy Physics, Chinese Academy of Sciences, 100039 Beijing, People's Republic of China; [g]School of Environmental Sciences and Engineering, Peking University, 100871 Beijing, People's Republic of China; [h]Department of Geosciences, Virginia Institute of Technology, Blacksburg, VA 24061; and [i]Subsurface Science and Technology Group, Energy and Environment Directorate, Pacific Northwest National Laboratory, Richland, WA 99352

Edited by Susan L. Brantley, Pennsylvania State University, University Park, PA, and approved March 26, 2019 (received for review February 13, 2019)

Sunlight drives photosynthesis and associated biological processes, and also influences inorganic processes that shape Earth's climate and geochemistry. Bacterial solar-to-chemical energy conversion on this planet evolved to use an intricate intracellular process of phototrophy. However, a natural nonbiological counterpart to phototrophy has yet to be recognized. In this work, we reveal the inherent "phototrophic-like" behavior of vast expanses of natural rock/soil surfaces from deserts, red soils, and karst environments, all of which can drive photon-to-electron conversions. Using scanning electron microscopy, transmission electron microscopy, micro-Raman spectroscopy, and X-ray absorption spectroscopy, Fe and Mn (oxyhydr)oxide-rich coatings were found in rock varnishes, as were Fe (oxyhydr)oxides on red soil surfaces and minute amounts of Mn oxides on karst rock surfaces. By directly fabricating a photoelectric detection device on the thin section of a rock varnish sample, we have recorded an in situ photocurrent micromapping of the coatings, which behave as highly sensitive and stable photoelectric systems. Additional measurements of red soil and powder separated from the outermost surface of karst rocks yielded photocurrents that are also sensitive to irradiation. The prominent solar-responsive capability of the phototrophic-like rocks/soils is ascribed to the semiconducting Fe- and Mn (oxyhydr)oxide-mineral coatings. The native semiconducting Fe/Mn-rich coatings may play a role similar, in part, to photosynthetic systems and thus provide a distinctive driving force for redox (bio)geochemistry on Earth's surfaces.

phototrophic | mineral coatings | birnessite | solar energy | redox (bio)geochemistry

Innumerable previous studies concerning the most critical influences of solar energy on the surface of this planet have mainly focused on its influence on Earth's climate (1), on photosynthesis and associated biological processes (2, 3), and on geological and soil processes (4). However, although widely exposed natural minerals on Earth's surface receive solar irradiation over very long time periods, the electronic response of these interactions and how this process also shapes the planet on which we live have rarely received attention.

Many decades of cutting-edge science have provided a deep understanding of biological light-harvesting capabilities that convert solar to chemical energy for the formation of biomolecules necessary for life. Such intricate purely organic processes are exhibited on this planet by chlorophyll- or rhodopsin-based phototrophic bacteria (5–7). Although laboratory arrangements for extracellular phototrophy with the aid of semiconducting minerals have succeeded in stimulating the growth of the iron-oxidizing bacterium *Acidithiobacillus ferrooxidans* (8) and the acetogens *Sporomusa ovata* (9) and *Moorella thermoacetica* (10, 11), no evidence has yet emerged for the widespread existence of a nonbiological component of a light-harvesting system that could be an inherent component of any portion of life on this planet. Finding a natural inorganic system that might deliver solar energy to nonphototrophic organisms in nature would imply a role, analogous to photosystem II (PS II) or rhodopsin, for novel modes of extracellular phototrophic metabolisms. Such a system would also provide a distinctive driving force for redox (bio)geochemistry on Earth's surfaces.

In this work, we provide field observations that widespread occurrences of rocks have thin coatings of Fe and Mn (oxyhydr)

Significance

In solar-terrestrial systems, solar energy input has long been recognized to have a profound impact on Earth. The well-known photosynthetic systems enable sustainable solar-to-chemical energy conversion. However, no evidence has yet emerged for the existence of a widespread geological light-harvesting system. This study reveals such a "photoelectric device," where semiconducting Fe- and Mn (oxyhydr)oxide-mineral coatings are found to overlay vast expanses of natural rock/soil surfaces and exhibit highly responsive and stable photon-to-electron conversion. Our discovery may provide insight supporting vital photon-induced redox chemistry on Earth's surface via widespread Fe- and Mn-mineral coatings.

Author contributions: A.L., Yan Li[3], H.D., and M.F.H. designed research; A.L., Yan Li[3], H.D., X.X., Yanzhang Li, G.R., J. Liang, Y. Liu, H.H., N.C., S.C., F.L., Yan Li[4], H.W., C.D., C.W., and K.L. performed research; Yan Li[3], Yanzhang Li, J. Liang, H.H., and K.L. contributed new reagents/analytic tools; A.L., Yan Li[3], H.D., X.X., Yanzhang Li, G.R., J. Liang, Y. Liu, H.H., N.C., S.C., F.L., Yan Li[4], H.W., C.D., Y. Lai, K.L., and M.F.H. analyzed data; and A.L., Yan Li[3], X.X., Yanzhang Li, J. Liang, Y. Liu, H.H., J. Liu, J.D., K.L., and M.F.H. wrote the paper.

The authors declare no conflict of interest.

This article is a PNAS Direct Submission.

[1]A.L., Yan Li[3], and H.D. contributed equally to this work.

[2]To whom correspondence may be addressed. Email: ahlu@pku.edu.cn, khliu@pku.edu.cn, or hochella@vt.edu.

[3]Associate Professor, Beijing Key Laboratory of Mineral Environmental Function, School of Earth and Space Sciences, Peking University, 100871 Beijing, People's Republic of China, and The Key Laboratory of Orogenic Belts and Crustal Evolution, School of Earth and Space Sciences, Peking University, 100871 Beijing, People's Republic of China.

[4]PhD student, Beijing Key Laboratory of Mineral Environmental Function, School of Earth and Space Sciences, Peking University, 100871 Beijing, People's Republic of China, and The Key Laboratory of Orogenic Belts and Crustal Evolution, School of Earth and Space Sciences, Peking University, 100871 Beijing, People's Republic of China.

This article contains supporting information online at www.pnas.org/lookup/suppl/doi:10.1073/pnas.1902473116/-/DCSupplemental.

Published online April 22, 2019.

oxides on their surfaces. By applying in situ photoelectric mapping measurements, the photocurrent generation of the Fe- and Mn (oxyhydr)oxide-mineral coatings was recorded and compared with that of the rock substrates. This study offers strong evidence that exposed land surfaces that are dominated by rocks are often "phototrophic-like" in their behavior, that is, purely inorganic, mineral systems. Vast expanses of rock surfaces exposed to sunlight are capable of harvesting and contributing to the conversion of solar energy to chemical energy and therefore driving chemical reactions.

Fe and Mn (Oxyhydr)oxide Thin Coatings on Earth's Surface

Widespread occurrences of rocks have thin coatings of Fe and Mn (oxyhydr)oxides on their surfaces (Fig. 1) (12–14). Such rocks often make distinctive landscapes in deserts (Fig. 1*A*), including the expansive Gobi region of China and Mongolia. Other examples include dark gray coatings on karst terrains (Fig. 1*D*) and reddish-yellowish or dark brown coatings covering soil particles (Fig. 1*G*). Rock varnish generally appears as a very dark (often black) coating that is well developed on bare rock surfaces in terrestrial arid and semiarid regions (Fig. 1*A*) (15, 16).

Mn-rich coatings are generally found only on upper rock surfaces that are exposed to solar light, while the undersides of rocks are reddish to yellowish (Fig. 1*A*, *Lower Right*). EDS mapping of Mn and Fe (Fig. 1 *B* and *H*) indicates that these two elements are enriched in the mineral coatings but not in the bulk rock. The Mn concentrations in rock varnish surfaces are often enriched by two orders of magnitude relative to the whole rock or soil particle and also the average crustal abundance of ~0.13 wt % (17). In contrast, the undersides of the same rocks mainly

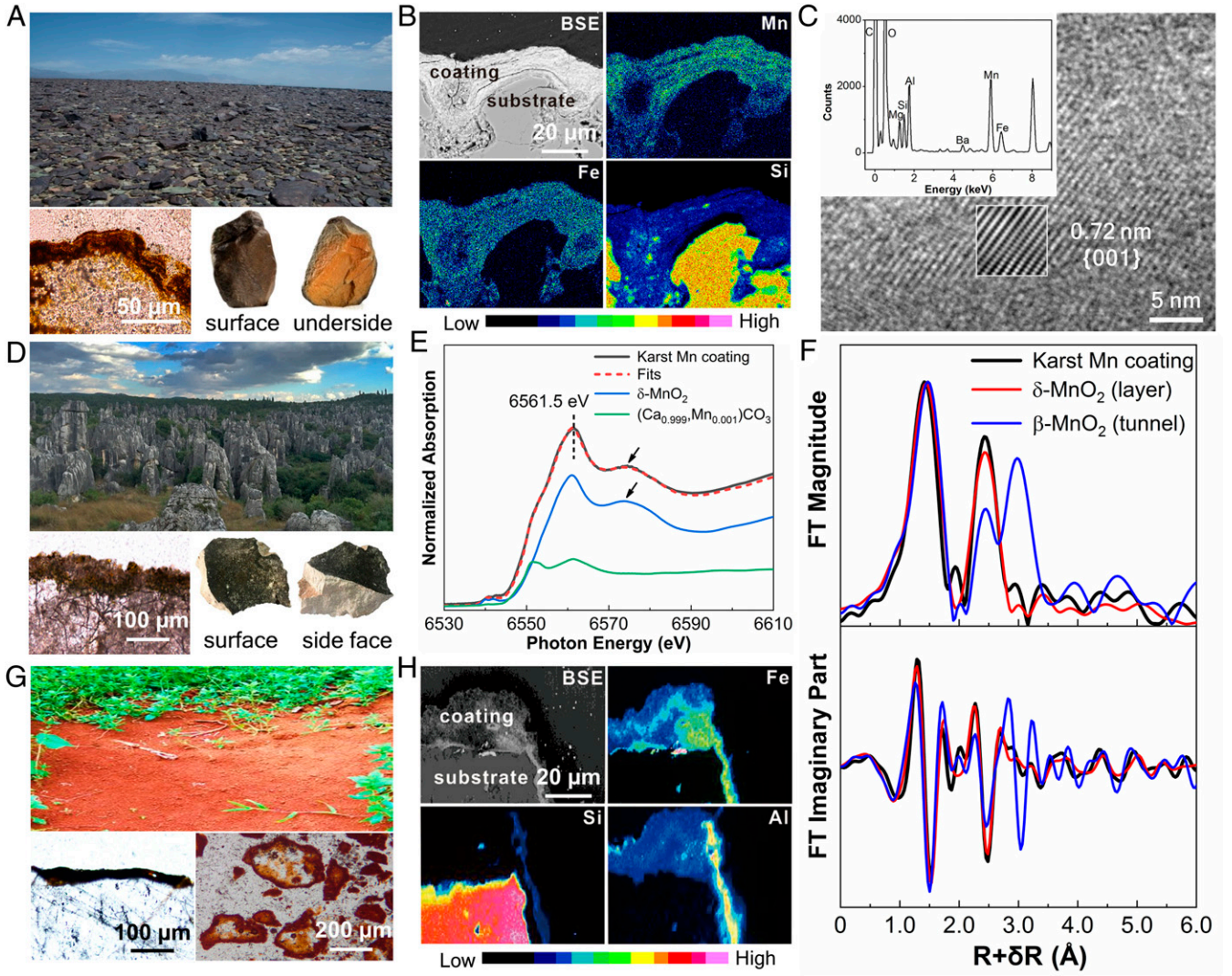

Fig. 1. (*A*) Representative landscape of the Gobi Desert in northwest China (*Upper*) with optical micrograph (*Lower Left*) showing mineral coatings and hand specimens (*Lower Right*) showing the color contrast between the surface and underside of rocks. (*B*) Backscattered electron (BSE) image of a rock thin section collected from the Gobi Desert and the corresponding elemental mapping of Mn, Fe, and Si by energy-dispersive X-ray spectroscopy (EDX). (*C*) HRTEM image of an Mn-rich coating from Gobi rock. The EDX spectrum (*Upper Inset*) corresponds to a spot in an Mn-rich region. Inverse fast Fourier transform image (*Lower Inset*) shows the clear lattice fringe. (*D*) Representative landscape of karst in southwest China (*Upper*) with an optical micrograph (*Lower Left*) and hand specimens (*Lower Right*) showing the color contrast between the surface and inside of rocks. (*E*) Normalized Mn *K*-edge XANES spectrum of a karst Mn coating and the least-squares fits using linear combination fitting of the spectra of δ-$Mn^{IV}O_2$ and $(Ca_{0.999}, Mn^{II}_{0.001})CO_3$. (*F*) FT magnitude (*Upper*) and imaginary part (*Lower*) derived from Mn *K*-edge EXAFS spectra of a karst Mn coating, synthetic δ-MnO_2 (layer structure), and β-MnO_2 (tunnel structure). (*G*) Representative landscape of the red soil region in southern China (*Upper*) with optical micrographs (*Lower Left* in polarized optical microscope and *Lower Right* in stereoscope). (*H*) BSE of a soil particle thin section collected from the red soil region and corresponding elemental mapping of Fe, Si, and Al by EDX.

consist of Fe (oxyhydr)oxides (i.e., hematite) with no Mn-rich minerals present (*SI Appendix*, Fig. S1). Rocks with a dark Mn-rich varnish are also generally found on the sunlit side of landforms, and Mn-poor rocks commonly occur on the shaded side (18, 19). In addition, the growth rate of Mn-rich coatings was found to be much faster in high-UV flux or photic environments (20, 21). Notably, the distribution of dark Mn-rich rock coatings overlaps the regions with strong solar irradiation (*SI Appendix*, Fig. S2). This pattern implies a close relationship between the formation of Mn oxides and solar light.

The high-resolution transmission electron microscopy (HRTEM) image (Fig. 1*C*) of Mn oxide on a Gobi rock surface exhibits a lattice fringe spacing of 0.72 nm, corresponding to the {001} plane of birnessite. Furthermore, the Raman spectra of the rock varnish have sharp peaks from the Mn−O stretching vibration modes of birnessite at 591 and 643 cm^{-1} (*SI Appendix*, Fig. S3). Tunneled Mn oxides are not identified, even though they typically have better crystallinity. In powders scratched from karst mineral coatings, the Mn content is less than 0.1 wt %, making it difficult to detect Mn species by X-ray diffraction, HRTEM, or Raman spectroscopy. Instead, X-ray absorption spectroscopy (XAS) was used for these samples. The normalized Mn *K*-edge X-ray absorption near-edge structure (XANES) spectrum of the karst Mn-rich coating displays a maximum absorption peak at 6,561.5 eV (Fig. 1*E*), followed by a broad shoulder feature at ∼6,574.5 eV (indicated by arrows); these absorbance features closely match those of δ-MnO_2, suggesting that the Mn local structure in karst Mn-containing coatings could predominantly be of the MnO_2 type. The least-squares linear combination fitting of the XANES spectrum gives 73(1)% δ-$Mn^{IV}O_2$ and 27(1)% $(Ca_{0.999}, Mn^{II}_{0.001})CO_3$, implying an average Mn oxidation state of ∼3.46. In the Fourier transform (FT) magnitude of the extended X-ray absorption fine structure (EXAFS) spectra (Fig. 1*F*, *Upper*), the second main peak at R+δR ∼ 2.5 Å can be attributed to Mn−Mn coordination where adjacent MnO_6 octahedra share edges with each other (22–24) and form a layer structure (25). The peak at R+δR ∼ 3.0 Å could arise from the Mn−Mn coordination of MnO_6 octahedra sharing corners, which occurs in tunnel-structure Mn oxides (22, 24, 25). The spectrum of the karst Mn-rich coating resembles layer-structure δ-MnO_2 more than tunnel-structure β-MnO_2, especially at ∼3.0 Å; furthermore, the FT imaginary part is more similar to that of layer-structure δ-MnO_2, particularly at ∼2.7 Å to ∼4.0 Å (Fig. 1*F*). These results suggest that the Mn oxides in this karst coating sample have mainly a layer structure.

Photoelectric Behavior of Fe and Mn (Oxyhydr)oxide Coatings

Layered Mn oxides have been reported as efficient catalysts in photochemical systems (26). Likewise, in situ photoelectric mapping measurements (Fig. 2 *A*–*D*) indicate that desert varnish samples are stable and sensitive photoelectric systems. A

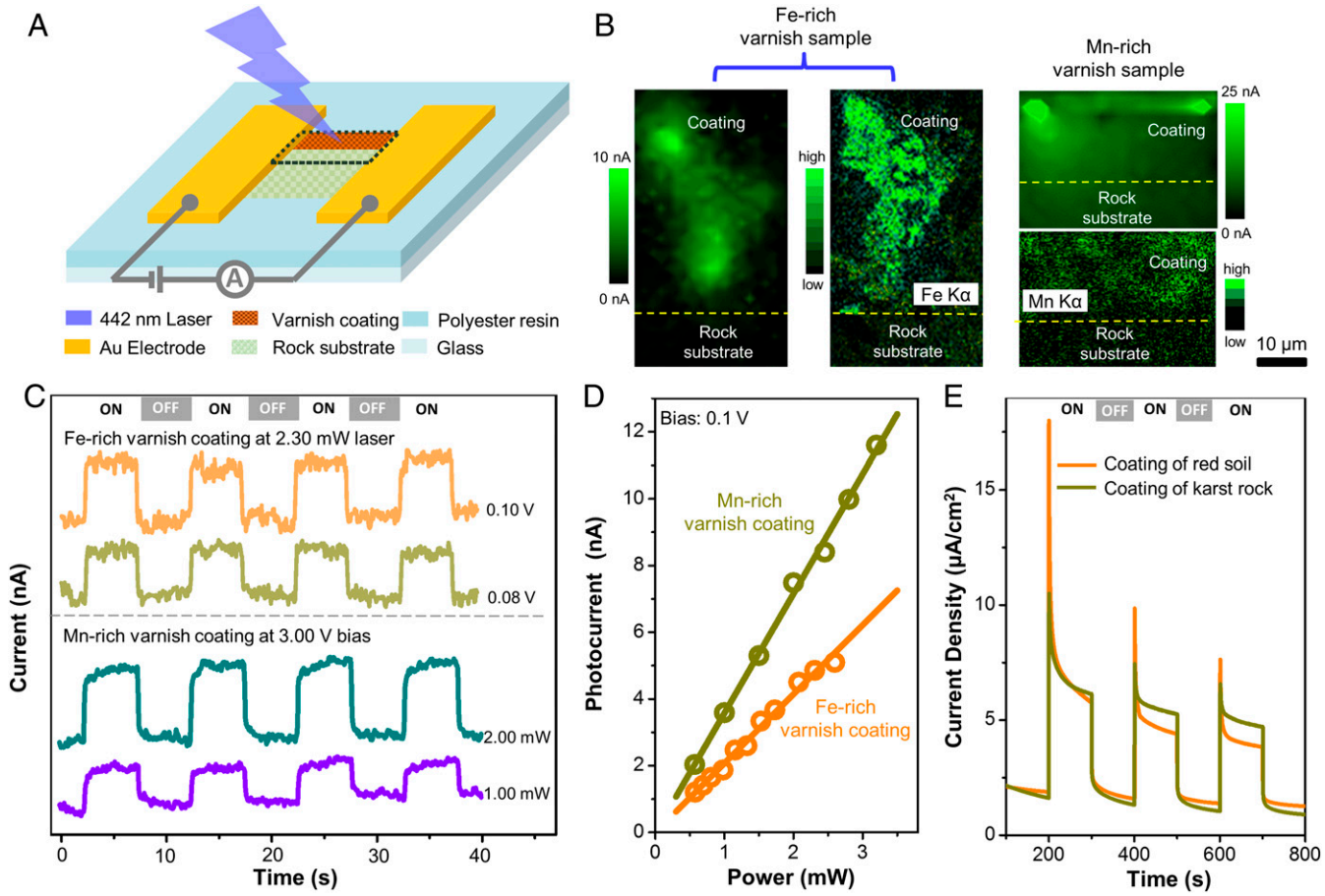

Fig. 2. Photoelectric measurement results of mineral coatings. (*A*) Schematic diagram of in situ photoelectronic measurement on a rock varnish sample. (*B*) Photocurrent and EDX micromapping of Fe-rich and Mn-rich varnish samples (the mapping region corresponds to the area marked by the black dashed line in *A*). (*C*) Photocurrent time curves collected from varnish samples and recorded at a selected bias or light intensity. (*D*) Good linear relationships between photocurrents collected from varnish samples and light intensity. (*E*) Photocurrent time behavior of electrodes fabricated by mineral coating powders from red soil and karst rock. ON and OFF represent the state of the light source.

photocurrent is detectable only in the region of the Fe- or Mn-rich mineral coating (Fig. 2*B*; additional elementary composition in *SI Appendix*, Fig. S4). When illuminating a spot in this area with a selected bias and laser power, the photocurrent is elevated in the "ON" state and immediately descends to the baseline in the "OFF" state (Fig. 2*C*), performing with high sensitivity and stability just like a natural photoelectric device. Notably, the photocurrent exhibits a close linear relationship with bias and laser power (Fig. 2*D* and *SI Appendix*, Fig. S5), demonstrating a constant photon-to-electron conversion efficiency. At a fixed bias of 0.1 V and 442-nm laser excitation (a wavelength in the violet range with a photon energy of 2.8 eV, able to promote an electron from the top of the valence band to the bottom of the conduction band of semiconducting minerals in mineral coatings), the estimated photoresponsivity is 2×10^{-6} A/W, and the effective quantum efficiency (EQE) is 5.8×10^{-6} for the Fe-rich coating, while there is 1.7-fold enhancement for the Mn-rich coating (for details, see *Materials and Methods*). Similarly, red soil and powder separated from the outermost surface of karst rocks yield photocurrents that are sensitive to irradiation (Fig. 2*E*). In contrast to the rock substrates and nonsemiconducting silicate minerals (quartz and feldspar), which do not produce photocurrents (Fig. 2*B* and *SI Appendix*, Fig. S6), the mineral coatings behave as natural photoelectric generators and show long-term stability (*SI Appendix*, Fig. S6).

The capability of photo-to-electric transduction in the desert varnish coatings may be ascribed to naturally occurring minerals, which are identified as mainly birnessite (triclinic and hexagonal types), hematite, and goethite (*SI Appendix*, Fig. S3). The bandgaps (E_g), as determined by oxygen *K*-edge absorption and emission spectra (Fig. 3*A*), are 2.57, 2.10, 1.82, and 1.77 eV for goethite, hematite, and hexagonal and triclinic birnessite, respectively, indicating that the coatings are all visible light-responding semiconducting minerals. A comparison of the redox potentials of H_2O and humic acid (HA) (27)—one of the most common compounds in natural organic matter—with the valence band edges of the four minerals (Fig. 3*B*) demonstrates the potential for H_2O and HA oxidation by photoexcited holes, allowing for the release of photoelectrons. In addition, many other compounds with reducing potentials, including dissolved transition metal ions, as well as a vast store of other inorganic and organic substances, are widespread in natural environments due to inexhaustible production by the decomposition of biomass or dissolution of minerals (28–30). These compounds can all serve as possible electron donors to scavenge positively charged photoholes generated by the photocatalysis of Fe- and Mn-mineral coatings and then facilitate the outflow of photoelectrons (31–34).

According to in situ photoelectricity tests of Mn-rich coatings, a photocurrent density of ~358 nA/cm^2 is generated when a varnish sample is irradiated by a simulated solar source with an average light intensity of 100 mW/cm^2 and a small bias of 0.1 V is applied. In total, an estimated 2.23×10^{16} photoelectrons can be produced per second from a 1-m^2 rock varnish-covered land surface under the current experimental conditions. Certainly, the amount of naturally produced photoelectrons is not uniform in varnish-covered areas, due to the uneven exposure to sunlight, availability of different electron donors, and distribution of mineral coatings. However, considering the vast rock varnish-covered land surface of 3.567×10^{13} m^2 (35), the global-scale production of photoelectrons emitted from the mineral coatings is not negligible. These photoelectrons could be a major source of extracellular electrical energy to fuel photoelectrotrophic bacteria (8, 36). Our findings substantiate the implications of laboratory experiments on extracellular phototrophy, which have succeeded in stimulating the bacterial growth of iron-oxidizing bacterium *A. ferrooxidans* (8) and the acetogens *S. ovata* (9) and *M. thermoacetica* (10, 11) with the aid of semiconducting photocatalytic minerals.

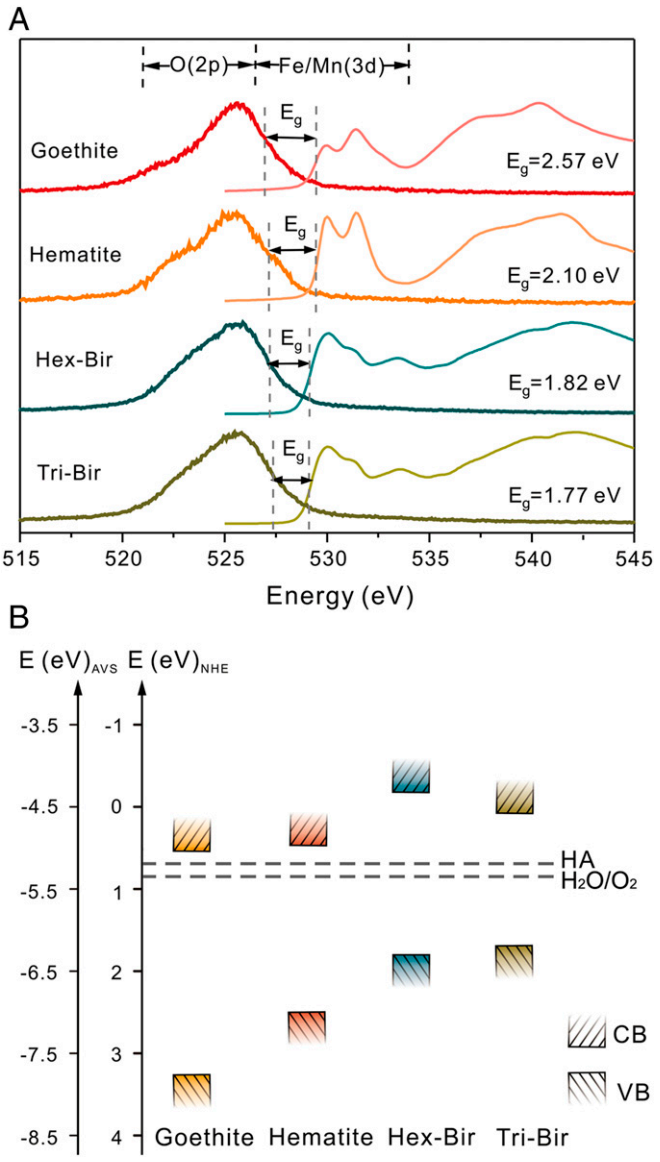

Fig. 3. The bandgap structure and redox potential of some semiconducting minerals in mineral coatings. (*A*) Oxygen *K*-edge absorption (thin lines) and emission spectra (bold lines) of Fe (oxyhydr)oxides and Mn oxides in the desert varnish coatings. The bandgap (E_g) of each mineral is determined by calculating the energy difference between the top of the valence band and the bottom of the conduction band given by the inflection points on the adsorption spectra and at half-peak height on the emission spectra. (*B*) Band edge positions of Fe (oxyhydr)oxides and Mn oxides with respect to the normal hydrogen electrode (NHE, V) and the absolute vacuum scale (AVS, eV). The upper rectangles represent the bottoms of the conduction bands, and the lower rectangles represent the tops of the valence bands (pH = 7). The dashed line indicates the redox potentials of HA (27) and H_2O/O_2 redox couples.

We conclude that the solar light response and photocurrent production of widespread semiconducting mineral coatings are capable of playing important roles in biogeochemical processes on Earth's surface (Fig. 4). It should be noted that Mn is especially concentrated in the "coating" layer. The valence band potential of the main Mn-bearing mineral in coatings, for example, birnessite, is more positive than the redox potential of H_2O/O_2 (Fig. 3), suggesting that the photocatalytic oxidation of water to oxygen may occur in the topmost layer of the geosphere (6). In addition, the photoelectrons from the conduction band of birnessite, similar to other semiconductors, can provide a driving force for

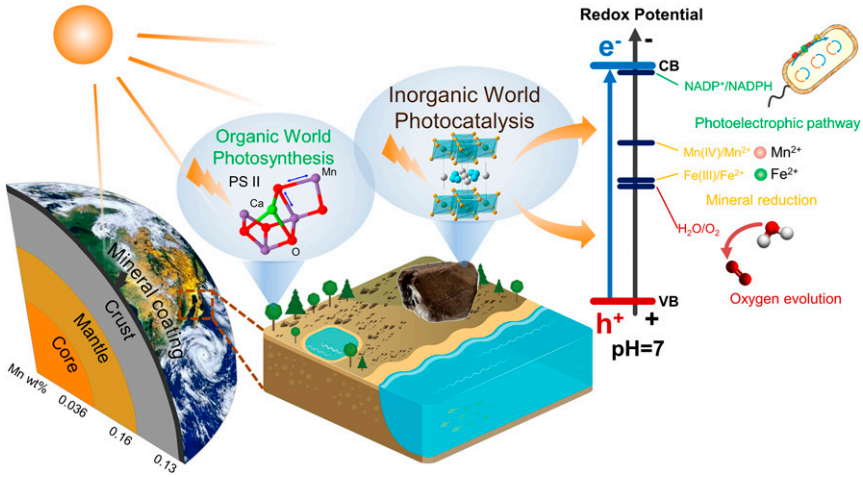

Fig. 4. Schematic model showing the topmost layer of Earth's semiconducting mineral coating together with PS II for harvesting and transforming solar energy. This coating lies parallel to the core, mantle, and crust, but clearly represents a vanishingly small amount of mass compared with these major Earth components/layers. Nevertheless, the average abundances of Mn in the core, mantle, and crust have low values, as indicated in this figure, while Mn is extraordinarily concentrated in the ultrathin layer of mineral coatings. These coatings, together with the PS II protein complex in oxygenic photosynthetic organisms, are believed to be responsible for harvesting and transforming solar energy in the geosphere and biosphere, respectively, which broadens the pathways for utilizing solar energy from the well-known organic world to the newly discovered mineral semiconductor world.

the reduction of elements such as iron and manganese (31, 32, 37), regenerate NADPH from $NADP^+$ (38), and provide a new form of energy for bacterial metabolisms (10, 36). The inexhaustible electron donors (e.g., water, organics, reduced ions) in nature can complete those electron transport chains and bring about continuous redox chemistry, in which the semiconducting mineral coatings act as the vital bridge. Overall, the solar harvesting and photoelectric converting properties of these coatings broaden the pathways for utilizing solar energy from the well-known organic world to the mineral semiconductor world.

Materials and Methods

Sample Collection and Preparation. Black rock varnishes on the surface of rock (bedrock: feldspar–quartz sandstone) were collected from Dushanzi, Xinjiang, China (41°49′04″N, 82°52′17″E). Gray-black desert rock varnishes (bedrock: quartz sandstone) in the Gobi region were collected from Hami, Xinjiang, China (43°17′37″N, 92°16′24″E). Black karst rocks (bedrock: limestone–dolomite) were collected from the surface of limestone in Shilin, Yunnan, China (24°4′40″N, 104°8′47″E). The substrates below those coatings, i.e., feldspar–quartz sandstone for desert varnish and limestone–dolomite for karst, were also collected for comparison. Red soil samples (soil parent material: granite) were collected from surface soil (0 cm to 2 cm) of Changsha, Hunan, China (30°42′N, 114°24′E). The silicate substrate of the red soil matrix was obtained by removing Fe and Mn oxides from its surface coating; that is, the red soil matrix was soaked in 1 M HCl for 30 min under ambient temperature and then washed by deionized water five times. After that, the samples were dried at 35 °C for 12 h. All samples were air-dried, cut along the vertical direction of the sample surface into impregnated blocks, and burnished into several thin sections of about 30 μm for observation under polarization optical microscope and environmental scanning electron microscope. Mineral coating powder samples were gently scratched away from rock substrates using tungsten carbide knives under an optical microscope, and were then crushed down to a particle size below 350 mesh. The mineral coating samples were observed under transmission electron microscope and characterized by XAS, aqueous photoelectrochemical measurements, Raman spectroscopy, zeta potential measurement, and oxygen *K*-edge absorption and emission spectra (XAS-XES). More details are available in *SI Appendix, Extended Materials and Methods*.

Synchrotron Radiation X-Ray Spectroscopy Analysis. Mn *K*-edge X-ray absorption data were collected on the Hard X-ray MicroAnalysis beamline (HXMA, 06ID) at the Canadian Light Source (CLS) (39). For the karst Mn coatings, the experiment was performed in fluorescence mode by using a Canberra 32 Ge germanium array detector. For the Mn-phase reference standards (including δ-MnO_2, β-MnO_2, acid birnessite, γ-MnOOH, Mn_2O_3, MnO, $MnCO_3$, and $MnSO_4{\cdot}H_2O$), the experiment was performed in transmission mode by using Oxford ion chamber detectors filled with 100% He gas. For the additional references of a series of calcite–rhodochrosite solid solution, i.e., $(Ca_x,Mn_{1-x})CO_3$, the experiment was performed under fluorescence mode. The in-step energy calibration was made by using an Mn metal foil set downstream of the sample. During the data collection, the storage ring at CLS was operated under 250 mA or 220 mA, and the superconducting wiggler source of the HXMA beamline was run at 1.7 T or 2.2 T.

The Mn *K*-edge raw data analysis was performed using the IFEFFIT software package according to the standard data analysis procedures (40). The spectral energy of all samples was uniformly calibrated with Mn foil. E_0 was set at the first inflection point on the absorption edge. The spectra were preedge background subtracted and postedge normalized using Athena program in IFEFFIT software package. The EXAFS spectra were k^2-weighted and converted to R space by FT over the k range of 3.3 $Å^{-1}$ to 10.8 $Å^{-1}$ using a Hanning window with *dk* set as 1 $Å^{-1}$. Linear combination fitting of XANES spectra of karst Mn coatings was done by Athena program in IFEFFIT using the least-squares method. All of the above Mn reference standards were used as fitting components. The fitting range was from −20 eV to 60 eV around the edge energy. More details are available in *SI Appendix, Extended Materials and Methods*.

XAS-XES was measured on station 10ID-2 at CLS. Synthetic Mn oxide samples (Hex- and Tri-birnessite) and Fe oxide samples (hematite, goethite) were dried, crushed in a mortar, and mounted directly into the holders. Slits were adjusted to 25 mm on the monochrometer and 25 mm on the spectrometer to give a resolution of 0.4 eV for the absorption spectra and 0.6 eV for the emission spectra. Experiments were carried out at vacuum pressures less than 10^{-9} torr.

In Situ Photoresponse Measurement of Desert Varnish Samples. The experiment was conducted on desert varnish thin sections with thicknesses of 30 μm. By combining standard electron beam deposition and shadow mask technology, two Ti/Au (5 nm/1 μm) electrodes with 20-μm channels were fabricated on the selected area, which simultaneously covered the mineral membrane, glue, and substrate, as shown in Fig. 2*A*. The in situ photoresponse of the rock was investigated by a 442-nm laser (Changchun New Industries Optoelectronics Technology Co., Ltd.), which was focused with a diameter of ∼1.8 μm through a 0.65-N.A. objective. A Keithley 2400 SourceMeter was used to provide bias and record the current between two electrodes at the same time. Light power was recorded by a PM100D-type Digital Power and Energy Meter Console equipped with an S120C-type sensor (Thorlabs). A homemade laser confocal microscope together with a piezo stage and controller (P-333.3CD and E-725; Physik Instrumente) was used for in situ photocurrent mapping. At each point, the currents in ON and OFF states were read separately, with photon shutter durations of off and on for 3 s; then the current difference was recorded to form a mapping before it was moved to the next point with 1-μm step size. When fixing a point, photoresponse signals were recorded under a selected bias and

light power. The detailed calculation about photoelectric density is available in *SI Appendix, Extended Materials and Methods*.

Calculation of EQE in Desert Varnish Samples. As illustrated in Fig. 2*D*, the fitting equation that describes the linear relationship between photocurrent (nanoampere per square centimeter) and light power (milliwatt per square centimeter) in Fe-rich Mn-rich coatings are presented as Eqs. **1** and **3**, respectively. According to these equations, the ratio of photocurrent to light power is a constant for both cases, making it possible to calculate the EQE based on Eqs. **2** and **4**, which helps to evaluate the capability of a photoelectric device for converting solar to electrical energy.

For Fe-rich coatings,

$$I_{Fe} = 2.07P \quad [1]$$

$$\mathrm{EQE} = \frac{n_e}{n_p} = \frac{I_{Fe}hc}{\lambda Pe} = \frac{2.07 \times 6.626 \times 10^{-34} \times 2.998 \times 10^{8}}{442 \times 1.602 \times 10^{-19} \times 10^{-3}} = 5.81 \times 10^{-6}. \quad [2]$$

For Mn-rich coatings,

$$I_{Mn} = 3.58P \quad [3]$$

$$\mathrm{EQE} = \frac{n_e}{n_p} = \frac{I_{Mn}hc}{\lambda Pe} = \frac{3.58 \times 6.626 \times 10^{-34} \times 2.998 \times 10^{8}}{442 \times 1.602 \times 10^{-19} \times 10^{-3}} = 1.00 \times 10^{-5}. \quad [4]$$

In Eqs. **1**–**4**, I, P, n_e, n_p, h, c, λ, and e represent the photocurrent (denoted as I_{Fe} for Fe-rich coatings and I_{Mn} for Mn-rich coatings), power of the light source, the number of generated photoelectrons, the number of incident photons, Planck constant, velocity of light, wavelength of incident laser, and elementary charge, respectively.

ACKNOWLEDGMENTS. We thank the beamline staffs in 06ID-1 (HXMA) and 10ID-2 (Resonant Elastic and Inelastic X-ray Scattering, REIXS) of CLS and 1W1B of Beijing Synchrotron Radiation Facility for help with X-ray absorption and emission spectroscopy measurements and data processing. This work was supported by National Key Basic Research Program of China Programs Grants 2014CB846001 and 2016YFA0300903; Natural Science Foundation of China Grants 41820104003, 41872042, 91851208, 41230103, 41522201, and 51522201; and Beijing Graphene Innovation Program Z181100004818003.

1. Foukal P, Fröhlich C, Spruit H, Wigley TML (2006) Variations in solar luminosity and their effect on the Earth's climate. *Nature* 443:161–166.
2. Dau H, Zaharieva I (2009) Principles, efficiency, and blueprint character of solar-energy conversion in photosynthetic water oxidation. *Acc Chem Res* 42:1861–1870.
3. Katan J (1981) Solar heating (solarization) of soil for control of soilborne pests. *Annu Rev Phytopathol* 19:211–236.
4. Doane TA (2017) A survey of photogeochemistry. *Geochem Trans* 18:1–24.
5. Des Marais DJ (2000) When did photosynthesis emerge on Earth? *Science* 289: 1703–1705.
6. Sauer K, Yachandra VK (2002) A possible evolutionary origin for the Mn_4 cluster of the photosynthetic water oxidation complex from natural MnO_2 precipitates in the early ocean. *Proc Natl Acad Sci USA* 99:8631–8636.
7. Béja O, et al. (2000) Bacterial rhodopsin: Evidence for a new type of phototrophy in the sea. *Science* 289:1902–1906.
8. Lu A, et al. (2012) Growth of non-phototrophic microorganisms using solar energy through mineral photocatalysis. *Nat Commun* 3:768.
9. Liu C, et al. (2015) Nanowire–bacteria hybrids for unassisted solar carbon dioxide fixation to value-added chemicals. *Nano Lett* 15:3634–3639.
10. Sakimoto KK, Wong AB, Yang P (2016) Self-photosensitization of nonphotosynthetic bacteria for solar-to-chemical production. *Science* 351:74–77.
11. Sakimoto KK, Zhang SJ, Yang P (2016) Cysteine–cystine photoregeneration for oxygenic photosynthesis of acetic acid from CO_2 by a tandem inorganic–biological hybrid system. *Nano Lett* 16:5883–5887.
12. Garvie LAJ, Burt DM, Buseck PR (2008) Nanometer-scale complexity, growth, and diagenesis in desert varnish. *Geology* 36:215–218.
13. Perry RS, Adams JB (1978) Desert varnish: Evidence for cyclic deposition of manganese. *Nature* 276:489–491.
14. Sarmast M, Farpoor MH, Boroujeni IE (2017) Soil and desert varnish development as indicators of landform evolution in central Iranian deserts. *Catena* 149:98–109.
15. Dorn RI (1991) Rock varnish. *Am Sci* 79:542–553.
16. Goldsmith Y, Stein M, Enzel Y (2014) From dust to varnish: Geochemical constraints on rock varnish formation in the Negev Desert, Israel. *Geochim Cosmochim Acta* 126: 97–111.
17. Taylor SR, McLennan SM (1985) *The Continental Crust: Its Composition and Evolution* (Blackwell Sci, Oxford).
18. Schindler M, Dorn RI (2017) Coatings on rocks and minerals: The interface between the lithosphere and the biosphere, hydrosphere, and atmosphere. *Elements* 13: 155–158.
19. Nealson KH (2015) Ex-phot: A new take on primitive utilization of solar energy. *Environ Microbiol Rep* 7:33–35.
20. Krinsley D, Dorn RI, DiGregorio B (2009) Astrobiological implications of rock varnish in Tibet. *Astrobiology* 9:551–562.
21. Koschinsky A, Hein JR (2017) Marine ferromanganese encrustations: Archives of changing oceans. *Elements* 13:177–182.
22. McKeown DA, Post JE (2001) Characterization of manganese oxide mineralogy in rock varnish and dendrites using X-ray absorption spectroscopy. *Am Mineral* 86:701–713.
23. Villalobos M, Lanson B, Manceau A, Toner B, Sposito G (2006) Structural model for the biogenic Mn oxide produced by *Pseudomonas putida*. *Am Mineral* 91:489–502.
24. Webb SM, Tebo BM, Bargar JR (2005) Structural characterization of biogenic Mn oxides produced in seawater by the marine *bacillus sp.* strain SG-1. *Am Mineral* 90: 1342–1357.
25. Post JE (1999) Manganese oxide minerals: Crystal structures and economic and environmental significance. *Proc Natl Acad Sci USA* 96:3447–3454.
26. Sakai N, Ebina Y, Takada K, Sasaki T (2005) Photocurrent generation from semiconducting manganese oxide nanosheets in response to visible light. *J Phys Chem B* 109:9651–9655.
27. Struyk Z, Sposito G (2001) Redox properties of standard humic acids. *Geoderma* 102: 329–346.
28. Dorn RI, Oberlander TM (1981) Microbial origin of desert varnish. *Science* 213: 1245–1247.
29. Becking LB, Kaplan IR, Moore D (1960) Limits of the natural environment in terms of pH and oxidation-reduction potentials. *J Geol* 68:243–284.
30. Edwards HG, Moody CA, Jorge Villar SE, Mancinelli R (2004) Raman spectroscopy of desert varnishes and their rock substrata. *J Raman Spectrosc* 35:475–479.
31. Sunda WG, Huntsman SA, Harvey GR (1983) Photoreduction of manganese oxides in seawater and its geochemical and biological implications. *Nature* 301:234–236.
32. Sherman DM (2005) Electronic structures of iron (III) and manganese (IV)(hydr) oxide minerals: Thermodynamics of photochemical reductive dissolution in aquatic environments. *Geochim Cosmochim Acta* 69:3249–3255.
33. Fan JX, Wang YJ, Fan TT, Cui XD, Zhou DM (2014) Photo-induced oxidation of Sb (III) on goethite. *Chemosphere* 95:295–300.
34. Lan S, et al. (2017) Mechanisms of Mn (II) catalytic oxidation on ferrihydrite surfaces and the formation of manganese (oxyhydr) oxides. *Geochim Cosmochim Acta* 211: 79–96.
35. Walker AS (1996) *Deserts: Geology and Resources* (Univ Michigan Library, Ann Arbor).
36. Lu A, et al. (2013) Photoelectrons from minerals and microbial world: A perspective on life evolution in the early Earth. *Precambrian Res* 231:401–408.
37. Matsunaga K, Ohyama T, Kuma K, Kudo I, Suzuki Y (1995) Photoreduction of manganese dioxide in seawater by organic substances under ultraviolet or sunlight. *Water Res* 29:757–759.
38. Guo JL, et al. (2018) Light-driven fine chemical production in yeast biohybrids. *Science* 362:813–816.
39. Jiang DT, Chen N, Sheng W (2007) Wiggler-base hard X-ray spectroscopy beamline at CLS. *AIP Conf Proc* 879:800–803.
40. Newville M (2001) IFEFFIT: Interactive XAFS analysis and FEFF fitting. *J Synchrotron Radiat* 8:322–324.